Available online at www.sciencedirect.com
SCIENCE DIRECT®
Journal of Computational Physics 196 (2004) 298–326
JOURNAL OF COMPUTATIONAL PHYSICS
www.elsevier.com/locate/jcp

An accurate tangential force–displacement model for granular-flow simulations: Contacting spheres with plastic deformation, force-driven formulation

L. Vu-Quoc *, L. Lesburg [1], X. Zhang [2]

Department of Mechanical and Aerospace Engineering, P.O. Box 116250, 231 MAE-A building, University of Florida, Gainesville, FL 32611-6250, USA

Received 25 February 2003; received in revised form 24 October 2003; accepted 24 October 2003

Abstract

An elasto-plastic frictional tangential force–displacement (TFD) model for spheres in contact for accurate and efficient granular-flow simulations is presented in this paper; the present TFD is consistent with the elasto-plastic normal force–displacement (NFD) model presented in [ASME Journal of Applied Mechanics 67 (2) (2000) 363; Proceedings of the Royal Society of London, Series A 455 (1991) (1999) 4013]. The proposed elasto-plastic frictional TFD model is accurate, and is validated against non-linear finite-element analyses involving plastic flows under both loading and unloading conditions. The novelty of the present TFD model lies in (i) the additive decomposition of the elasto-plastic contact area radius into an elastic part and a plastic part, (ii) the correction of the particles' radii at the contact point, and (iii) the correction of the particles' elastic moduli. The correction of the contact-area radius represents an effect of plastic deformation in colliding particles; the correction of the radius of curvature represents a permanent indentation after impact; the correction of the elastic moduli represents a softening of the material due to plastic flow. The construction of both the present elasto-plastic frictional TFD model and its consistent companion, the elasto-plastic NFD model, parallels the formalism of the continuum theory of elasto-plasticity. Both NFD and TFD models form a coherent set of force–displacement (FD) models not available hitherto for granular-flow simulations, and are consistent with the Hertz, Cattaneo, Mindlin, Deresiewicz contact mechanics theory. Together, these FD models will allow for efficient simulations of granular flows (or granular gases) involving a large number of particles.

* Corresponding author. Tel.: +1-352-392-6227; fax: +1-352-392-7303.
E-mail address: vu-quoc@ufl.edu (L. Vu-Quoc).
URL: http://www.mae.ufl.edu/~vql.
[1] Now with Parametric Technology Corp. (PTC), Needham, MA.
[2] Now with Siemens Corp., Princeton, NJ.

0021-9991/$ - see front matter © 2003 Published by Elsevier Inc.
doi:10.1016/j.jcp.2003.10.025

1. Introduction and literature review

Many natural and industrial processes involve particle systems. Debris flows or lahars in volcanic regions [3], the mixing of dry granular powders in the manufacturing of pharmaceuticals [4] are some examples. The motion of such particle systems must be well understood to avoid potential losses of human lives and material damage in natural disasters, or to increase the efficiency of industrial processes in particle handling and transportation.

Simulation by the discrete element method (DEM) is an approach that can be used to increase the understanding of particle systems [5]. In DEM, models for direct particle–particle contacts, which dominates the behavior of the flow, play a crucial role. It has been amply demonstrated in [6] that an accurate tangential force–displacement (TFD) model would produce sharply different statistics of force amplitude and frequency of collision in dry granular flows; these quantities are critical, for example in the prediction the rate of attrition of the colliding particles due to particle breakage or particle fragmentation [7,8]. It is therefore important to use a model that can accurately describe the contact force–displacement (FD) relationship to obtain reliable simulation results. Since DEM is computationally intensive—especially when the number of particles is large—the FD models employed must also be efficient. A clear and detailed overview of the numerical approach employed in DEM and the role of the contact FD models in granular-flow simulations is given in [9].

In many particle systems, the inelastic behavior of the materials involved must be accounted for to provide a more accurate modeling of the overall system. In granular gas systems, it is important to model the inelastic nature of interparticle collisions [10], which provide a dissipation mechanism that steadily removes the kinetic energy from the system and leads to several non-equilibrium processes [11]. Although inelastic collisions of granular particles was modeled using viscoelasticity in [10] with an intention to apply to collision of ice balls [12], the elasto-plastic response of materials in collision or in dry friction must be accounted for in many other systems: Dissipative heavy-ion collisions [13], dry friction of solids [14,15], granular flows [16–18], etc.

Most existing FD models for DEM simulations are based on theories of contact mechanics. For example, the Hertz theory [19] provides solutions for elastic contact between spheres subjected to a normal load; and the Mindlin–Deresiewicz (MD) theory [20] provides solutions for elastic-frictional contact between spheres subjected to a frictional contact force in the tangential direction. Experimental and finite element (FE) verification of the stress distributions predicted by Hertz theory are provided in [21]. More recently, extensive FE validation of the Hertz and MD [20] theories is presented in [22]. The significant effect of plastic deformation on the FD relationships, as shown in [22], demonstrates the severity of a common deficiency among the models that are based on elastic contact mechanics theories: These models only account for elastic deformation in the FD relationship. Applying these models to the simulations of dry granular flows, in which most contacts involve plastic deformation, can lead to inaccurate results, particularly in the magnitude of the interparticle forces and the frequency of contact, as these quantities affect the rate of attrition of the colliding particles, as already mentioned above (see also [6]). For more effects of plastic deformation during contact, see also [23,24], both of which presented finite-element analysis (FEA) results for the normal indentation of elasto-plastic half-spaces by rigid spheres.

The FD relationship for a contact problem can be divided into three components in different directions related to the contact surface: normal, tangential, and spin. In the present paper, we focus on the TFD relation, which plays a similar important role as the normal force–displacement (NFD) relation on the amplitude of the interparticle forces and the frequency of collision in granular flows. Apart from the MD [20] theory for the elastic-frictional contact of two spheres in the tangential direction, a TFD model based on the formalism of elasto-plasticity was developed in [25]. Although developed based on an elasto-plasticity formalism, the model in [25] was applicable to elastic materials only. Other existing TFD models, such as those proposed in [26,27], and in [6], can be viewed as various approximations and simplifications to the

MD [20] theory. These TFD models do not account for the effect of plastic deformation. Moreover, there has been no previous work in the literature on frictional elasto-plastic TFD models.

In [2] and [1], we present an accurate and efficient elasto-plastic NFD model in a displacement-driven version and a force-driven version, respectively. In the present paper, we focus on the frictional elasto-plastic TFD model that is consistent with the formalism set forth in our previous work on elasto-plastic NFD models, and consistent with the Hertz, Cattaneo, Mindlin, and Deresiewicz theory for frictional elastic contact.

The novelty of the present TFD model lies in (i) the additive decomposition of the elasto-plastic contact area radius into an elastic part and a plastic part, (ii) the correction of the particles' radii at the contact point, and (iii) the correction of the particles' elastic moduli. The correction of the contact-area radius represents an effect of plastic deformation in colliding particles; the correction of the radius of curvature represents a permanent indentation after impact; the correction of the elastic moduli represents a softening of the material due to plastic flow. The proposed elasto-plastic frictional TFD model is accurate, and is validated against non-linear FE analyses involving plastic flows under both loading and unloading conditions.

2. Elastic-frictional contact

In this section, we review the contact mechanics theory of elastic-frictional contact between two spheres. This theory is at the foundation of our proposed elasto-plastic frictional TFD model.

2.1. Cattaneo, Mindlin, Deresiewicz theory

Hertz theory gives the NFD relationship for contacting spheres subjected to normal force [19]. Based on Hertz theory, the problem of contacting spheres subjected to a constant normal force and a varying tangential force was first considered in [28] and then independently in [29]. Later, in [20], the solution for the *simple-loading* [3] cases of two spheres in elastic-frictional contact subjected to a varying oblique force (as shown in Fig. 1) was presented. For the Cattaneo, Mindlin, Deresiewicz (CMD) theory of contact mechanics, the following assumptions are applied (see Fig. 2):

1. The normal pressure p acting between the spheres is given by Hertz theory. That is, the application of a tangential force changes neither the size of the contact area nor the normal pressure acting on it. In addition, the normal displacement of the spheres is also given by Hertz theory, and is independent of the tangential force.
2. Slip starts at the edge of circular contact area, and progresses with increasing Q toward the center of the contact area. The resulting slip zone is a circular annulus that is concentric with the contact area.
3. In the slip region, the tangential traction is given by the Coulomb friction limit $q = \mu p$, where μ is the friction coefficient.
4. The direction of slip is parallel to the direction of the applied tangential load Q. While components of slip do exist in directions that are not parallel to Q, the effect of these components is neglected.

Assumption 1 implies that the assumptions made in Hertz theory still hold, e.g., the contact area and the normal displacement are small, compared to the size of the contacting spheres. It was also indicated in [29] that if there were no slip on the contact surface, the tangential traction q at the outer edge of the circular contact area would go to infinity. Since real materials cannot sustain infinite traction, some slip must occur.

[3] We refer the reader to [20] and to [6] for the definition of *simple loadings*.

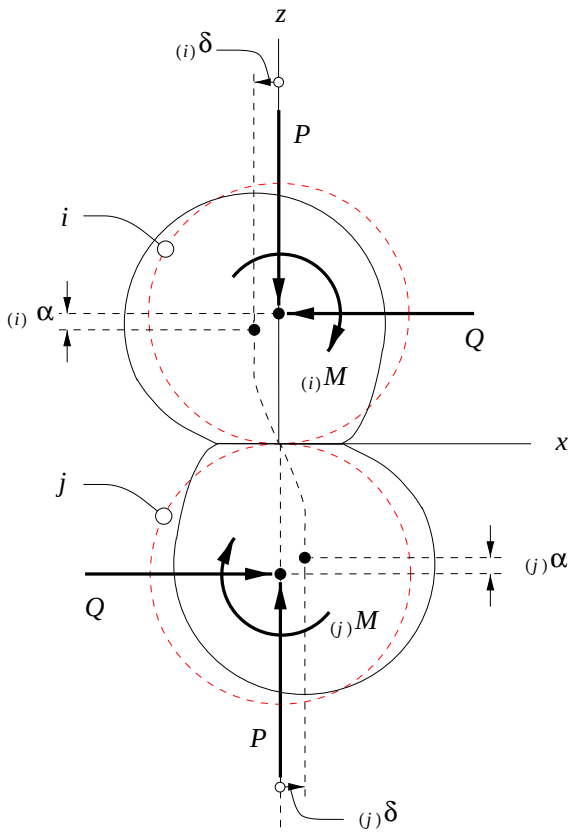

Fig. 1. Two spheres in contact and subjected to normal and tangential forces.

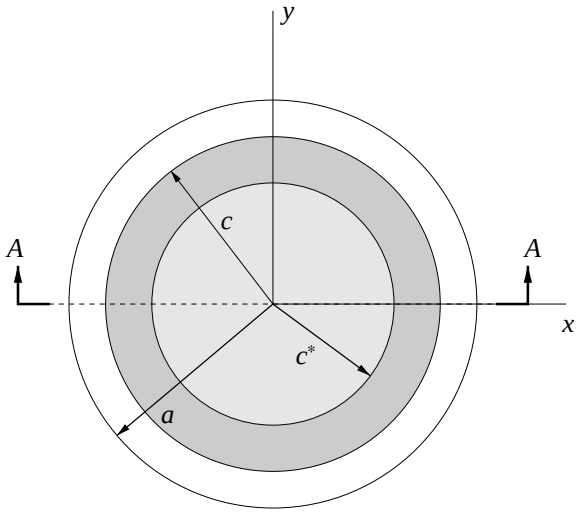

Fig. 2. Elastic-frictional contact: contact area (view from $+z$).

In what follows, we will discuss some cases of elastic-frictional contact between two spheres subjected to both normal and tangential forces, based on the CMD theory. For simplicity, we will restrict our discussion to the case of identical spheres (see Fig. 1), where ${}_{(i)}R = {}_{(j)}R = R$. Also, we assume that the spheres are homogeneous and made of the same material.

2.1.1. Case P constant, Q oscillating

At first, we load the two contacting spheres with only the normal force P. From Hertz theory, the contact-area radius a and the normal displacement α in each of the two spheres are given by

$$a = \left(\frac{3PR(1-\nu^2)}{4E}\right)^{1/3}, \quad \alpha = \frac{a^2}{R} = \left(\frac{9P^2(1-\nu^2)^2}{16RE^2}\right)^{1/3}, \tag{2.1}$$

where E and ν are the Young's modulus and Poisson's ratio of the sphere material, respectively. The normal pressure distribution p on the contact surface and the maximal normal pressure p_{m} are given by

$$p(r) = p_{\mathrm{m}}\left[1 - \left(\frac{r}{a}\right)\right]^{1/2}, \quad p_{\mathrm{m}} = \frac{3P}{2\pi a^2} = \left(\frac{6PE^2}{\pi^3 R^2(1-\nu^2)^2}\right)^{1/3}, \tag{2.2}$$

where r is the distance from the center of the contact area.

While holding the normal force P constant, we add a tangential force Q to the spheres, see Fig. 1. In accordance with Assumption 2, the stick region of the contact area is a circle of radius c (see Fig. 2). According to the theory of Cattaneo and Mindlin (CM), the radius c of the stick region can be expressed as

$$c = a\left(1 - \frac{Q}{\mu P}\right)^{1/3}, \tag{2.3}$$

where μ is the coefficient of friction. Outside the stick region, the value of tangential traction is equal to the friction limit μp; thus micro slip occurs in this *slip region*.

Cattaneo and Mindlin found that the tangential traction q on the contact surface can be expressed as

$$q = \begin{cases} \dfrac{3\mu P}{2\pi a^3}(a^2 - r^2)^{1/2}, & c \leqslant r \leqslant a, \\ \dfrac{3\mu P}{2\pi a^3}[(a^2 - r^2)^{1/2} - (c^2 - r^2)^{1/2}], & r \leqslant c. \end{cases} \tag{2.4}$$

Combining (2.4) with $(2.1)_1$ and the relation $G = \frac{1}{2}E/(1+\nu)$, the tangential traction can be expressed using the two-argument CM function σ_{CM} defined in [30] as

$$q = \sigma_{\mathrm{CM}}(a,c) := \begin{cases} \mathscr{C}(a^2 - r^2)^{1/2}, & c \leqslant r \leqslant a, \\ \mathscr{C}[(a^2 - r^2)^{1/2} - (c^2 - r^2)^{1/2}], & r \leqslant c, \end{cases} \tag{2.5}$$

where

$$\mathscr{C} := \frac{4\mu G}{\pi R(1-\nu)}. \tag{2.6}$$

The two-argument CM function $\sigma_{\mathrm{CM}}(\cdot,\cdot)$ has the following property

$$\sigma_{\mathrm{CM}}(a,b) + \sigma_{\mathrm{CM}}(b,c) = \sigma_{\mathrm{CM}}(a,c). \tag{2.7}$$

Property (2.7) can be used to simplify the application of the superposition method employed in the future analysis of CMD theories.

The tangential displacement of the center of the sphere relative to the contact area is then given in terms of Q by

$$\delta = \frac{3(2-\nu)\mu P}{16Ga}\left[1-\left(1-\frac{Q}{\mu P}\right)^{2/3}\right], \tag{2.8}$$

where G is the shear modulus of the sphere material. The *tangential stiffness* K_{T} can thus be obtained by taking the inverse of the differentiation of (2.8) with respect to Q to yield

$$K_{\mathrm{T}} = \left(\frac{\partial\delta}{\partial Q}\right)^{-1} = \frac{8Ga}{2-\nu}\left(1-\frac{Q}{\mu P}\right)^{1/3}. \tag{2.9}$$

Evaluating (2.9) at $Q = 0$, we find the initial-loading tangential stiffness

$$K_{\mathrm{T},0} = (K_{\mathrm{T}})_{Q=0} = \frac{8Ga}{2-\nu}, \tag{2.10}$$

which will prove to be an important expression in the subsequent exposition of the theory. At $Q = \mu P$ in (2.9) the tangential stiffness K_{T} goes to zero, as does the stick-area radius c in (2.3), and thus *free sliding* occurs.

Now consider the case where tangential force Q decreases to $Q = Q^* + \Delta Q$ after having monotonically increased to Q^* under the constant normal loading P. Assume that $Q^* \leqslant \mu P$, and that at $Q = Q^*$ the stick radius of the contact area is c^* (see Fig. 2). When the increment $\Delta Q(< 0)$ of tangential force is applied, the tangential traction on the contact surface is equivalent to the tangential traction q^* superposed with the corresponding tangential traction increment Δq as shown in Fig. 3. To avoid infinite traction at the outer edge of the contact area, the application of ΔQ must result in micro slip at the edge of the contact area, opposite in direction to that of q^*. In accordance with the CM theory, the radius c of the reverse slip region is given by

$$c = \left(1-\frac{Q^*-Q}{2\mu P}\right)^{1/3}. \tag{2.11}$$

At this point the tangential traction caused by the maximum tangential force Q^* is $q^* = \sigma_{\mathrm{CM}}(a, c^*)$, and the reverse traction caused by ΔQ is $\Delta q = -2\sigma_{\mathrm{CM}}(a, c)$. Therefore, we obtain the summation

$$q = q^* + \Delta q = \sigma_{\mathrm{CM}}(a, c^*) - 2\sigma_{\mathrm{CM}}(a, c). \tag{2.12}$$

The tangential displacement at Q can be expressed by

$$\delta = \frac{3(2-\nu)\mu P}{16Ga}\left[2\left(1-\frac{Q^*-Q}{2\mu P}\right)^{2/3} - \left(1-\frac{Q}{\mu P}\right)^{1/3} - 1\right]. \tag{2.13}$$

Differentiating (2.13) with respect to Q and taking the inverse of the derivative, we obtain the tangential stiffness expression for unloading

$$K_{\mathrm{T}} = \frac{8Ga}{2-\nu}\left(1-\frac{Q^*-Q}{2\mu P}\right)^{1/3}. \tag{2.14}$$

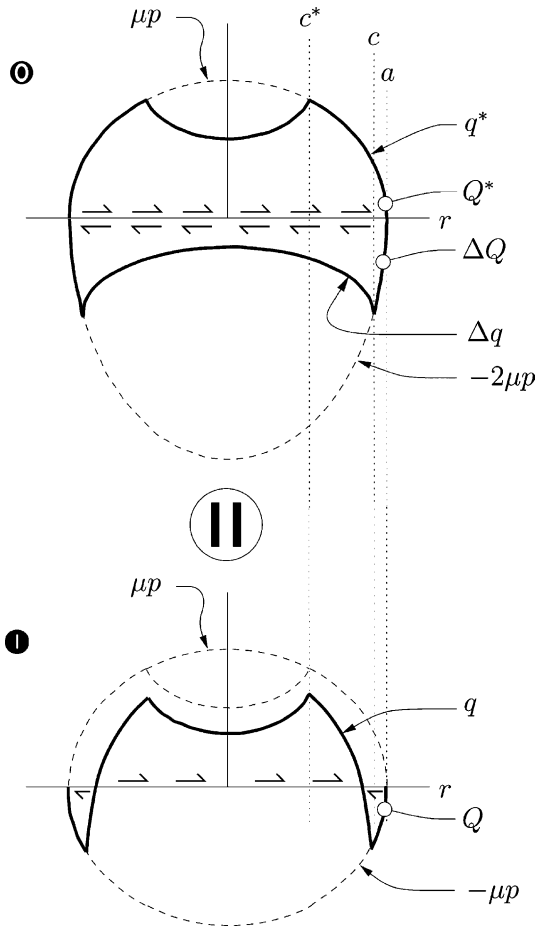

Fig. 3. Elastic-frictional contact: tangential tractions at Section *A–A* for P constant, Q decreasing.

Evaluating (2.14) at $Q = Q^*$, we obtain

$$K_{\mathrm{T},*} = (K_{\mathrm{T}})_{Q=Q^*} = \frac{8Ga}{2-\nu}. \tag{2.15}$$

Therefore, the initial unloading tangential stiffness $K_{\mathrm{T},*}$ is identical to the initial loading tangential stiffness in (2.10). From now on, we use $K_{\mathrm{T},0}$ for both loading and unloading tangential stiffness.

Fig. 4 shows the TFD curve for the cases with P constant and Q varying. The FD state ❶ shown in Fig. 4 corresponds to the case with P constant and Q decreasing as discussed above. As the tangential force Q decreases to zero, the tangential displacement δ decreases to a non-zero value δ_{r}, which is the residual tangential displacement. As a result, energy is dissipated. The area inside the hysteresis loop is equal to the energy dissipation of in one cycle of the tangential force.

In real impact problems, the normal force does not remain constant. An incremental method was applied to determine the stiffness (inverse of the compliance) expressions for identical spheres that were subjected to varying normal and tangential forces [20]. A *simple loading history* is a time history of P and Q such that, when each load is applied incrementally, the tangential traction after each increment is exactly the same as the tangential traction after an initial (or virgin) tangential-force loading or after a series of loading and unloading, all under a *constant* normal force.

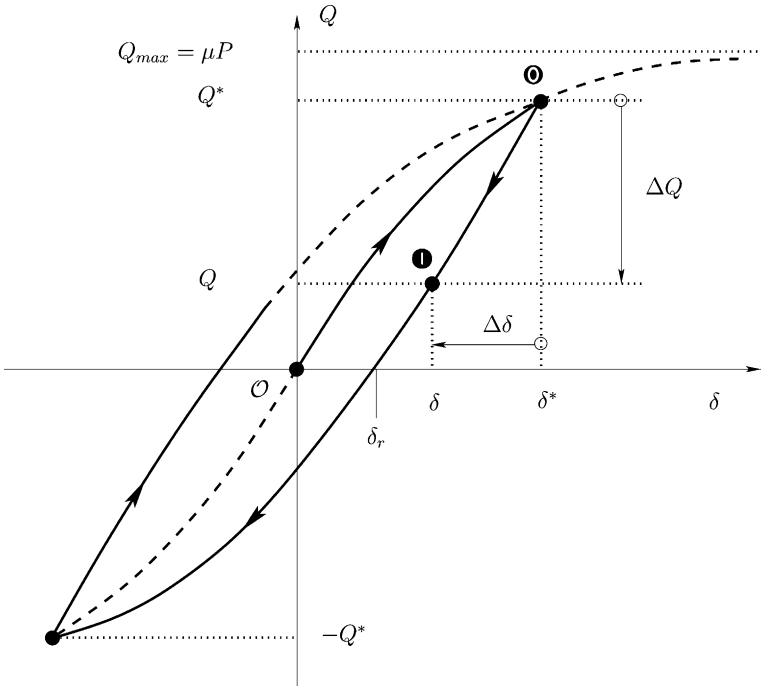

Fig. 4. Elastic-frictional contact: TFD curve for P constant, Q varying.

2.1.2. Case P increasing, Q increasing

Assume that the given initial state 0 with $\{P_0, Q_0, \delta_0\}$ shown in Fig. 5 is a result of a simple loading history; the corresponding tangential traction q_0 and initial friction limit μp_0 are both shown in Fig. 6.

When both the increment in normal force and the increment in tangential force are small, the final state 2 can be reached by first incrementing the normal force to $P_1 = P_0 + \Delta P$, and then by incrementing the tangential force to $Q_2 = Q_0 + \Delta Q$. When the normal force is increased to P_1, the radius a_1 of contact area is enlarged, the normal traction p_1 is increased everywhere on the contact area, and the friction limit is increased to μp_1 accordingly, as shown in Fig. 6. When the friction limit of the tangential traction is $\mu p_1 > \mu p_0 \geqslant q_0$ everywhere on the contact area, there is no longer any micro slip on the contact surface.

When the tangential force is increased to $Q_2 = Q_0 + \Delta Q$, two situations are observed: $\Delta Q \geqslant \mu \Delta P$, or $\Delta Q < \mu \Delta P$.

Subcase $\Delta Q \geqslant \mu \Delta P$: the increment ΔQ of tangential force can be decomposed into two parts: $\Delta Q = \Delta Q_{01} + \Delta Q_{12}$, with $\Delta Q_{01} = \mu \Delta P$ corresponding to state 1 shown in Figs. 5 and 6. Since there is no tangential traction on the newly created contact area $r \in [a_0, a_1]$, and since there is no micro slip on the entire contact area before the application of ΔQ_{01}, the distribution of ΔQ_{01} creates an additional tangential traction Δq_{01}, which is identical to the case where ΔQ_{01} is an initial loading of the tangential force under the constant normal force P_1. The stick radius for the incremental tangential traction distribution Δq_{01} due to the incremental tangential force ΔQ_{01} is actually equal to the radius a_0 of the whole contact area in state 0, due to (2.3) and $(2.1)_1$. (See the second subfigure in Fig. 6.) After a superposition of Δq_{01} onto q_0, the resulting traction $q_1 = q_0 + \Delta q_{01}$ is exactly the same as the tangential traction caused by holding P_1 constant and by increasing Q from zero to $Q_1 = Q_0 + \mu \Delta P$. We say the loading history is *simple* because we recover the state of tangential distribution obtained as if the normal load has always been constant at P_1. At this state 1, the tangential traction at any point in $c_0 \leqslant r \leqslant a_1$ is equal to the friction limit at that point. When

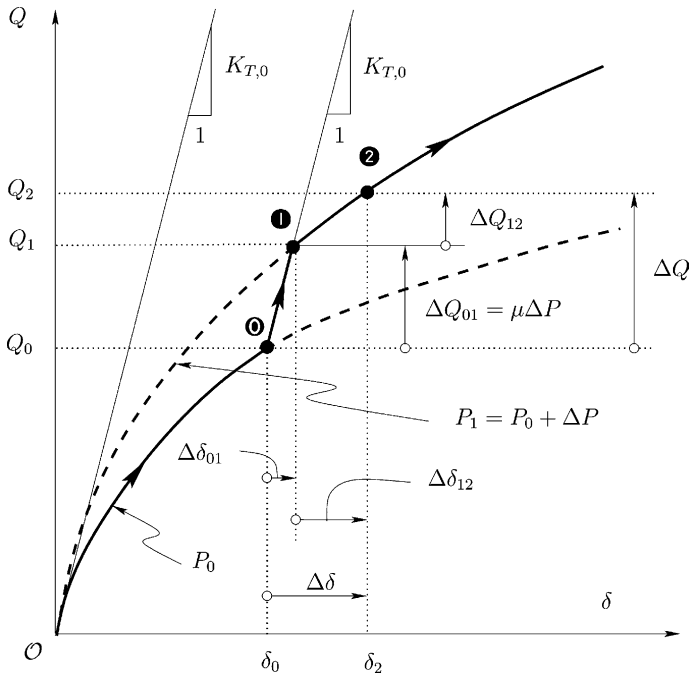

Fig. 5. Elastic-frictional contact: TFD curves for P increasing, Q increasing.

superposing the incremental tangential traction distribution Δq_{01} with stick area radius a_0 on the tangential traction distribution q_0 with stick area radius c_0, the stick-area radius in state ❶ remains c_0. The tangential displacement δ_1 at state ❶ can be expressed as

$$\delta_1 = \delta_0 + \Delta\delta_{01} = \delta_0 + \frac{\mu \Delta P}{(K_{\mathrm{T},0})_{P=P_0}}. \tag{2.16}$$

The next step is to apply the increment ΔQ_{12}. As shown in Figs. 5 and 6, from state ❶ to state ❷, the TFD relation is the same as that of a virgin tangential loading under the normal force P_1. The tangential displacement δ_2 at state ❷ can be expressed by

$$\delta_2 = \delta_1 + \Delta\delta_{12} = \delta_1 + \frac{\Delta Q_{12}}{K_{\mathrm{T},12}}, \tag{2.17}$$

where the tangential stiffness $K_{\mathrm{T},12}$ can be determined according to (2.9) by

$$K_{\mathrm{T},12} = \frac{8Ga}{2-\nu}\left(1 - \frac{Q_0 + \mu\Delta P}{\mu P_1}\right)^{1/3}. \tag{2.18}$$

The change of the tangential traction can be expressed as a series of superpositions of CM functions: At state ⓪, the tangential traction is $q_0 = \sigma_{\mathrm{CM}}(a_0, c_0)$. The tangential traction caused by the tangential force ΔQ_{01} is $\Delta q_{01} = \sigma_{\mathrm{CM}}(a_1, a_0)$. Therefore, we have the following tangential traction at state ❶ by superposition

$$q_1 = \sigma_{\mathrm{CM}}(a_0, c_0) + \sigma_{\mathrm{CM}}(a_1, a_0) = \sigma_{\mathrm{CM}}(a_1, c_0), \tag{2.19}$$

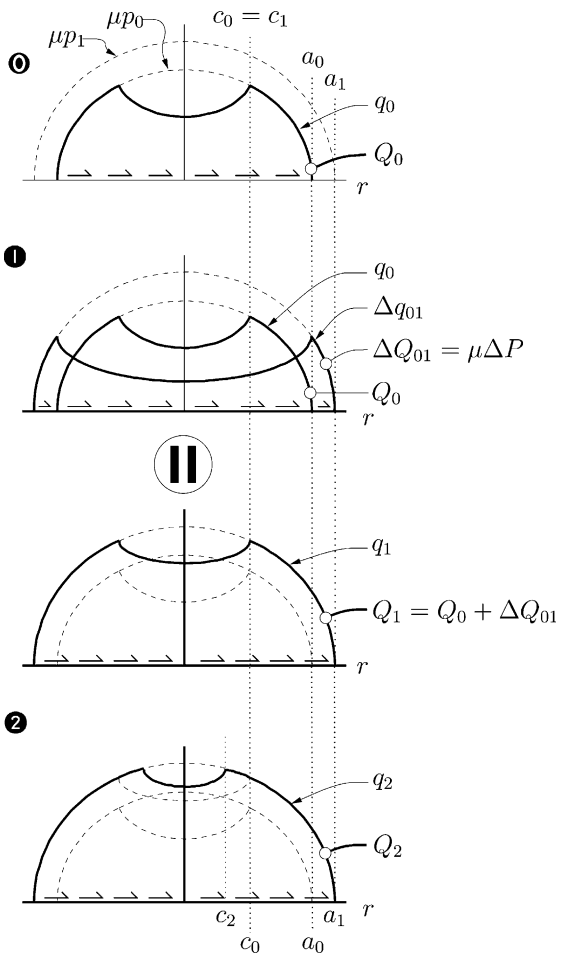

Fig. 6. Elastic-frictional contact: tangential tractions for P increasing, Q increasing ($\Delta Q \geqslant \mu \Delta P$).

where the second equality was obtained by using (2.7) in (2.19). Consequently, the tangential traction at state ❷ can be expressed by a two-argument CM function as

$$q_2 = \sigma_{\mathrm{CM}}(a_1, c_2). \tag{2.20}$$

Subcase $\Delta Q < \mu \Delta P$: This subcase is similar to the first step in going from state ⓪ to state ❶, as shown in Figs. 5 and 6. Since $\Delta Q < \mu \Delta P$, the stick-area radius of the incremental tangential traction Δq cannot develop enough to reach the former contact-area radius a_0 at state ⓪. Therefore, the tangential traction on the contact surface cannot return to that of a virgin tangential loading under a constant normal force, and thus the loading is no longer *simple*. The tangential displacement at this point can be expressed as

$$\delta_2 = \delta_0 + \frac{\Delta Q}{(K_{\mathrm{T},0})_{P=P_1}}. \tag{2.21}$$

If shown in Fig. 5, the final state would be a point between ⓪ and ❶.

More details about the change of the tangential and normal tractions, tangential stiffness, and the TFD relationship for other cases, such as (i) *P decreasing*, *Q increasing*, (ii) *P increasing*, *Q decreasing*, (iii) and *P decreasing*, *Q decreasing*, of simple loading histories can be found in [20].

A TFD model for elastic frictional contact based on the four (4) basic loading cases of the MD [20] theory has been implemented in our DEM granular flow simulation code [6]. The TFD model proposed in [6] has been validated with a large number of impact conditions and flow regimes. The present elasto-plastic frictional TFD model is a generalization of the elastic frictional TFD model in [6] to account for the effects of plastic deformation. The present TFD model is intended to be used for general loading histories. Again, only the four basic loading cases as discussed in [6] are considered in the development of the present TFD model.

2.2. FEA validation of CMD theory

Since tangential force and tangential displacement are involved, three dimensional FEA is necessary. We discretized a region of two identical spheres near the contact area, as shown in Fig. 7, where more than 3000 3-D FEs were used. The radius of the identical spheres is $R = 0.1$ m. The material properties chosen for the elastic contact were: Young's modulus $E = 7.0 \times 10^{10}$ N/m^2, Poisson's ratio $\nu = 0.3$, and coefficient of friction $\mu = 0.2$. In the following, we discuss some of the results obtained from our FEA using ABAQUS. We refer the readers to reference [22] for more details on our FEA model and the FEA results.

In the first test, we began by applying the normal contact force to $P = 2600$ N, and held this force constant. The tangential force was increased from zero to $Q = 500$ N, then decreased to zero under the constant normal force.

Fig. 8 shows the NFD curve when the normal force was applied. The FEA results agree well with the NFD curve obtained from Hertz theory by using $(2.1)_2$. At $P = 2600$ N, the maximum normal displacement from the FEA results differs from that of the Hertz theory by about 6.0%, which is larger than the difference (less than 1.0%) between Hertz theory and FEA results obtained using axisymmetric FEA, as presented in [1,22]. This larger error could be attributed to the following reasons: (i) the axisymmetric FEA model has a much finer mesh than the 3-D model shown in Fig. 7, (ii) the discretized region of a sphere in this 3-D FEA

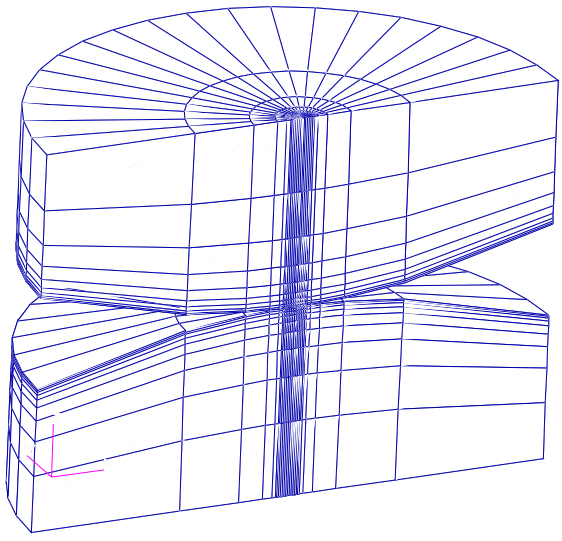

Fig. 7. 3-D FE mesh for two identical spheres in elasto-plastic frictional contact.

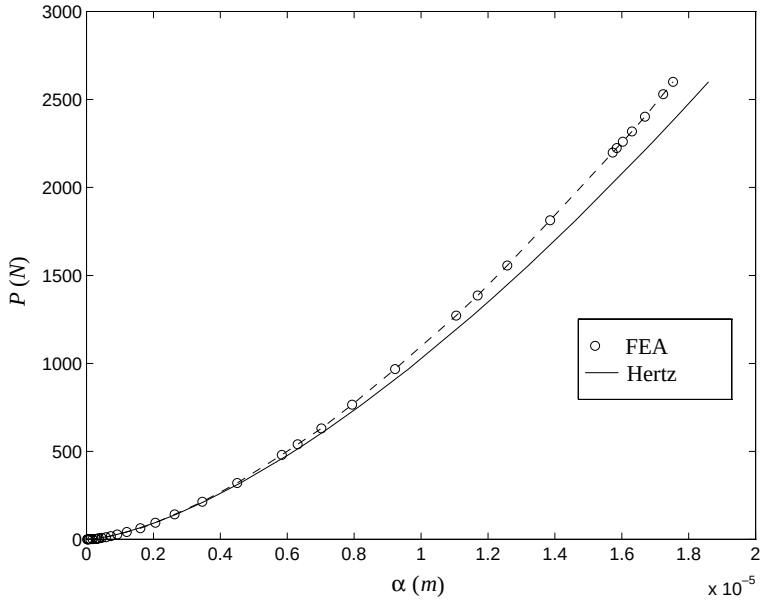

Fig. 8. Elastic-frictional contact: normal force P versus normal displacement α, for $P_{\max} = 2600$ N.

model is smaller than that in the axisymmetric FEA, and (iii) the axisymmetric FEA by its nature is less sensitive to discretization than full 3-D FEA.

Fig. 9 shows the TFD curve from the FEA results, which agree closely with the TFD curve obtained from the Cattaneo–Mindlin theory using (2.8) and (2.13). The maximum difference between the FEA results and the Cattaneo–Mindlin theory shown in Fig. 9 is less than 2.0%.

Figs. 10 and 11 show the normal traction and the tangential traction on the contact surface at $Q_{\max} = 500$ N under constant $P = 2600$ N, respectively. In Fig. 10, the FEA normal traction (pressure) p on the contact surface agrees well with the normal pressure from the Hertz theory, except for the value at the center of the contact area. Similarly, Fig. 11 shows the FEA tangential traction q agrees with the tangential traction from the Cattaneo–Mindlin theory, except for the value at the center of the contact area.

The computed values of the normal and tangential tractions at the center of the contact area are roughly *twice* the corresponding exact theoretical values. This numerical problem is attributed to the postprocessing algorithm employed in ABAQUS; such algorithm can be improved to avoid this numerical problem. The details on the use of ABAQUS to obtain these results are given in [22, p. 6483]. We note that a similar peculiar numerical behavior exists in the axisymmetric FEA as reported in [22, Fig. 7, p. 6463]; in this case, the computed normal traction at the center of the contact area as obtained from ABAQUS is about *half* of (instead of twice) the expected value.

A reason for the non-symmetric distribution of the shear stress τ_{xz} inside the layer of elements that are closest to the contact surface, as shown in Fig. 11 is likely due to the superposition of (i) the axisymmetrically distributed shear stress generated by the normal force pushing the two spheres toward each other and (ii) the non-symmetric distribution of shear stress generated by the tangential force.

Now consider a case where both P and Q are varying. Using the FEA model shown in Fig. 7, we start with the application of a normal force of $P = 400$ N. Next, we increase the tangential force with a constant rate from zero to $Q_{\max} = 360$ N, and at the same time increase the normal force also with a constant rate from 400 N to $P_{\max} = 2000$ N. When tangential force is unloaded from $Q_{\max} = 360$ N to zero, the normal

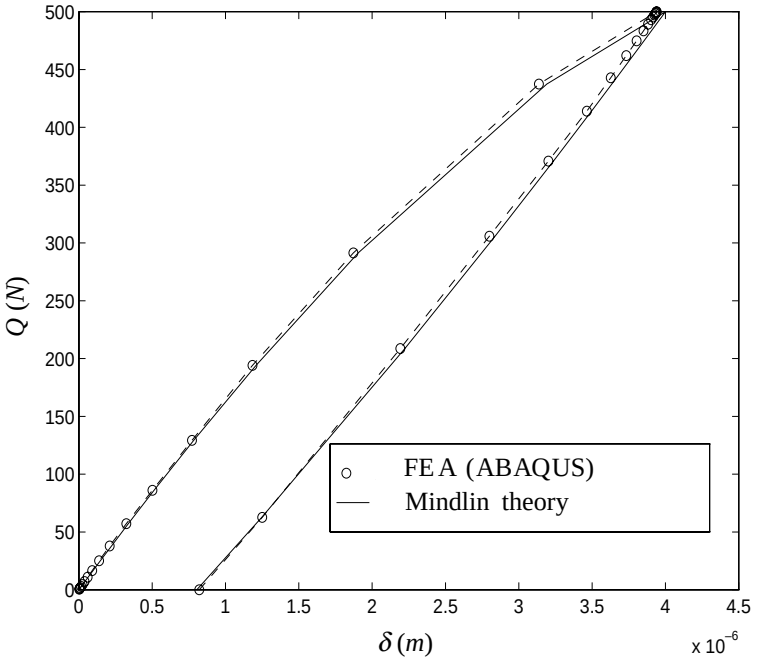

Fig. 9. Elastic-frictional contact: Q vs. δ, with $Q_{\max} = 500$ N under constant $P = 2600$ N.

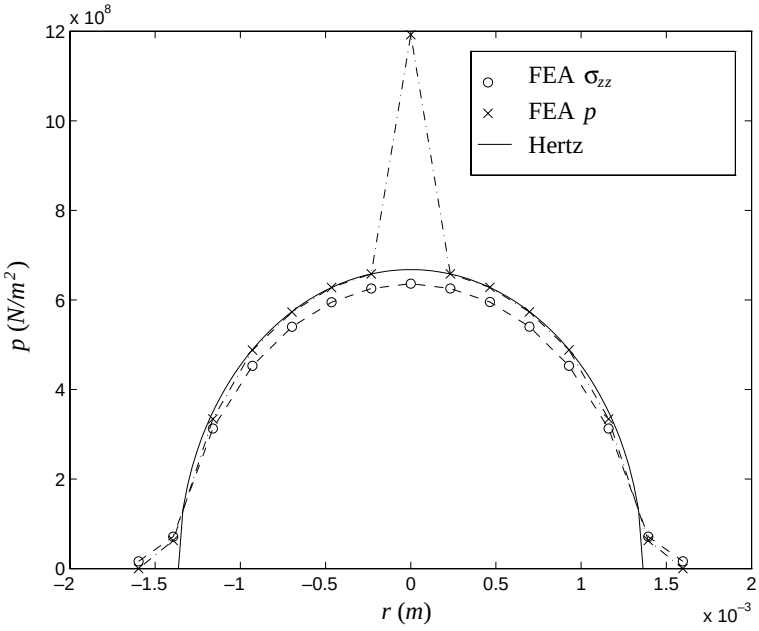

Fig. 10. Elastic-frictional contact: normal traction p and principal stress σ_{zz} at $P = 2600$ N.

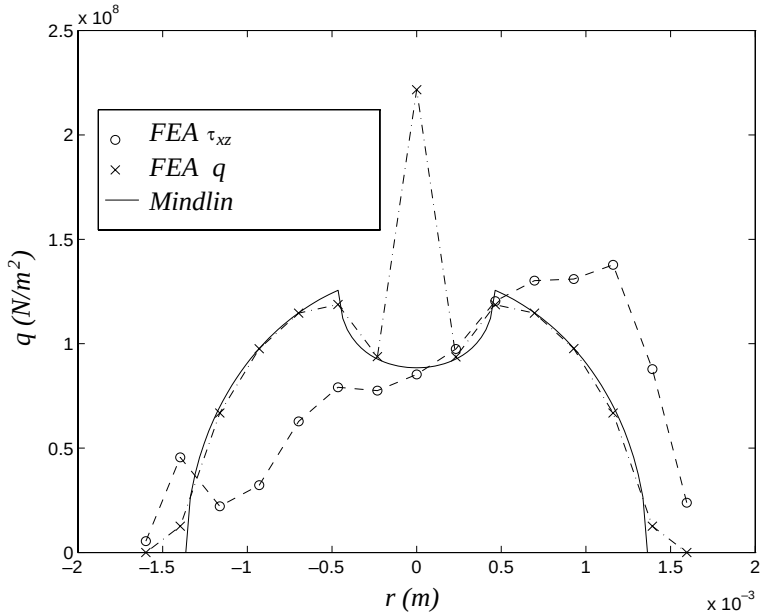

Fig. 11. Elastic-frictional contact: tangential traction q and shear stress τ_{xz} at $Q_{\max} = 500$ N.

force is unloaded from $P_{\max} = 2000$ N to $P = 400$ N accordingly. Fig. 12 shows that the TFD curve from FEA results agrees closely with the TFD curve from the MD [20] theory. What we have above is a simple loading history since $|\Delta Q| \geqslant \mu|\Delta P|$ throughout the tangential loading and unloading.

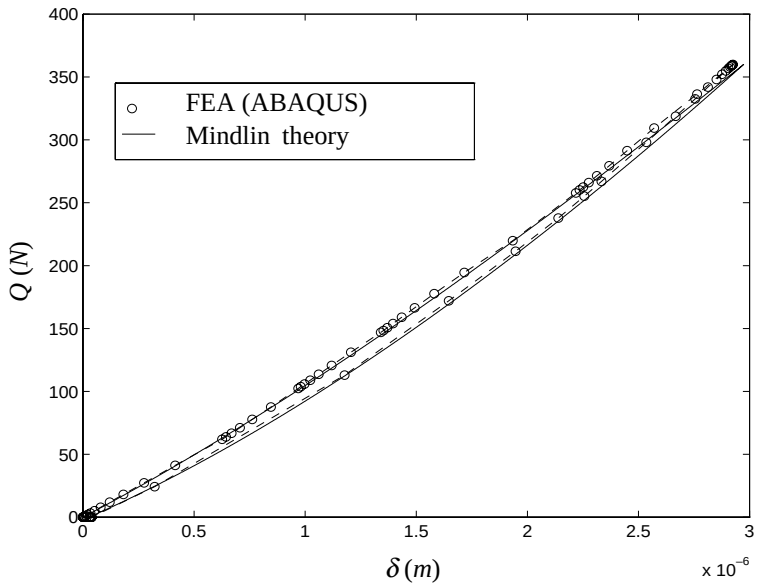

Fig. 12. Elastic-frictional contact: Q versus δ, for Q and P both varying. $Q_{\max} = 360$ N and $P_{\max} = 2000$ N.

Applying various loading histories to the FEA model shown in Fig. 7, we obtained FEA results that agree closely with the CMD theory [22]. From the comparisons between the FEA results and the CMD theory, we can conclude that (i) the CMD theory is accurate for elastic-frictional contact subjected to simple loading history, and (ii) the FEA model is reliable for the analysis of elastic-frictional contact problems. We will therefore use the discretization shown in Fig. 7 for further analysis of elasto-plastic contact problems.

We also carried out FEA for elastic-frictional contact subjected to non-simple loading histories, and found that the MD [20] theory is invalid for non-simple loading histories. The related results are presented in [6].

Although the FEA results for elastic-frictional contact presented in this section show that the CMD theory provides a correct TFD relationship, the application of CMD theory is limited to the cases when the contact area is much smaller than the size of the spheres in contact, i.e., $a \ll R$. Some of our other FEA results reveal that such condition is more rigorous for the CMD theory than for Hertz theory in the normal direction. For example, when $a \approx 0.01R$, the FEA results agree with Hertz theory but differ from the MD [20] theory by about 17% in the maximum tangential displacement.

3. Elasto-plastic TFD model: construction

We present the construction of an elasto-plastic TFD model in this section. There has never been any work in the literature dealing with the effects of plastic deformation on the TFD relations. Our work is a first attempt to tackle the problem. [4] The present elasto-plastic TFD model is based on the same formalism employed in the construction of the elasto-plastic NFD model in [1]; these two models thus provide a complete set of consistent elasto-plastic FD models for particles in collision.

3.1. FEA of elasto-plastic contact

We carried out the 3-D FEA of static contact problems of two identical elastic-perfectly-plastic spheres in frictional contact using the FEA mesh shown in Fig. 7. The geometric and elastic properties of the two spheres are the same as those used for the FEA of elastic contact, i.e., $R = 0.1$ m, Young's modulus $E = 7.0 \times 10^{10}$ N/m^2, Poisson's ratio $v = 0.3$, and the coefficient of friction $\mu = 0.2$. The uniaxial yield stress of the sphere material is set to $\sigma_Y = 1.0 \times 10^8$ N/m^2. From the FEA results (Figs. 9, 13, 14, and others presented in [22]), we observed the following FD behavior of the tangential contact stiffness:

- When the material is in the elastic range, i.e., without yield and plastic deformation, the FD behavior in the normal direction follows the Hertz theory; the FD behavior in the tangential direction follows the MD [20] theory.
- For the elastic-perfectly-plastic material employed in [22], the plastic deformation is mainly caused by normal force P, i.e., the shape and size of the plastic zone caused by both P and Q is very close to the one formed under only the same level of normal force P; but the plastic deformation *does* affect the TFD behavior.
- If the normal force is increased to a level that is much larger than the yield normal force P_Y (i.e., $P \gg P_Y$), and is then held constant before the application of the tangential force, even though there is a large amount of plastic deformation involved, the FD behavior in the tangential direction is a little stiffer than that from the MD [20] theory for the elastic case. Fig. 13 shows such a situation, where an aluminum sphere of radius $R = 0.1$ m, in contact with a frictional rigid planar surface, is subjected to a constant normal force $P = 2600$ N $\gg P_Y$ ($= 36.45$ N) and a varying tangential force Q; it can be observed that the FEA TFD relation is stiffer than the TFD relation in the MD [20] theory.

[4] The technical work in this paper was accomplished in Aug 1997, as reported in Lesburg's Master's thesis [35], the contents of which have been published in [1,22], and in the present paper. See also Zhang's PhD thesis [36], which was completed in Dec 1998. We have continued to work to publish our several research results obtained prior to Dec 1998 while carrying out our other research works.

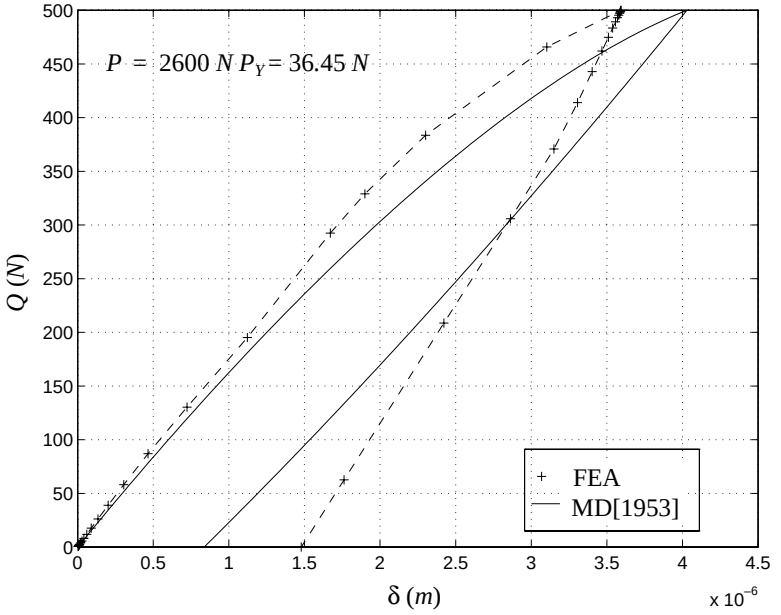

Fig. 13. Elasto-plastic frictional contact: Q vs. δ from FEA and [20] for $P = 2600$ N $\gg P_Y$ and Q varying.

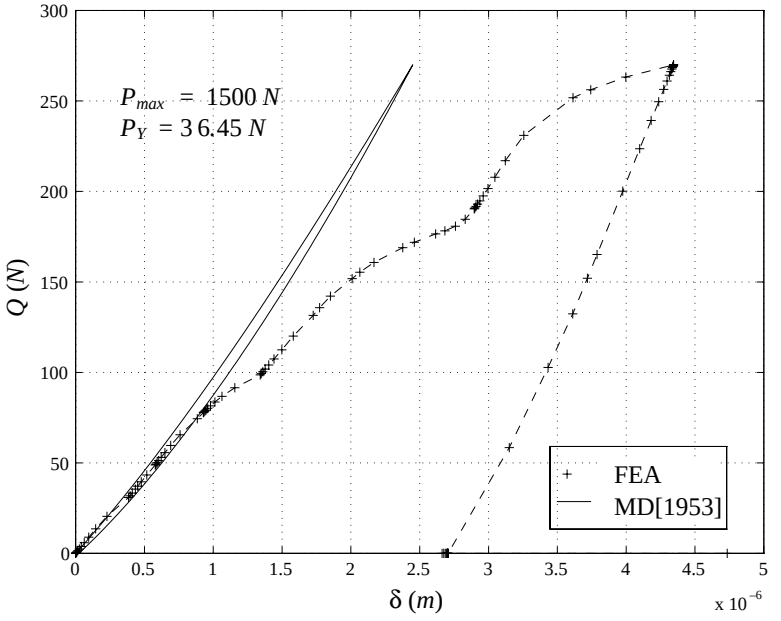

Fig. 14. Elasto-plastic frictional contact: Q vs. δ from FEA and [20] for P and Q vary, with $P_{\max} = 1500$ N.

- When both the normal force P and tangential force Q are applied at the same time, plastic deformation results in FD curves that are softer than those predicted by elastic contact mechanics theories. That is, the NFD curves are softer than those predicted by Hertz theory and follow softening trends that are

described in [2]. The TFD curves form hysteresis loops that are larger and softer than those observed for elastic cases. Fig. 14 shows a typical Q-versus-δ curve from elasto-plastic FEA results compared with the corresponding Q-versus-δ curve from the MD [20] theory for elastic contact.

We see that the plastic deformation increases the tangential stiffness in some cases, while decreases the tangential stiffness in some other cases. Such behavior is caused by two effects of plastic deformation. The first is that plastic deformation increases the contact area, thus a larger frictional surface is involved to resist the tangential force, thus causing the tangential stiffness to increase. On the other hand, plastic flow weakens the stiffness of the material involved, and thus decreases the tangential stiffness. An analogy that can be used to explain the behavior caused by plastic deformation, as just described above, is a column with changeable width shown in Fig. 15. The increase of the contact area is similar to the increase of the column width, and the weakening of the material caused by plastic deformation is similar to the necking that decreases the stiffness of the column. In certain cases, the increasing of the contact area plays a more important role; in these cases, the overall tangential contact stiffness increases. In other cases, when the weakening of the material by the plastic deformation is more significant, the overall tangential contact stiffness decreases.

The TFD curves shown in Fig. 14 correspond to the loading history $\mathbb{A}$ shown in Fig. 17 and Table 1. There are some 'bumps' in the TFD curve of FEA results shown in Fig. 14. These 'bumps' could be mainly the result of the plastic zone reaching the contact surface of the sphere, thus creating an additional sliding mechanism. Since the plastic deformation is mainly caused by the normal loading, when the normal force is a constant, as in the case shown in Fig. 13, there is no 'bump' on the TFD curve. For the case shown in Fig. 14, both the normal force and the tangential force are increased simultaneously. In this case, when the normal force reaches a certain level, the plastic zone is expanded to reach the contact surface and the center of the contact area is surrounded by a plastic zone, thus making it very easy for large displacements to occur. Further investigations into the numerical methods employed (e.g., properties of the FE used,

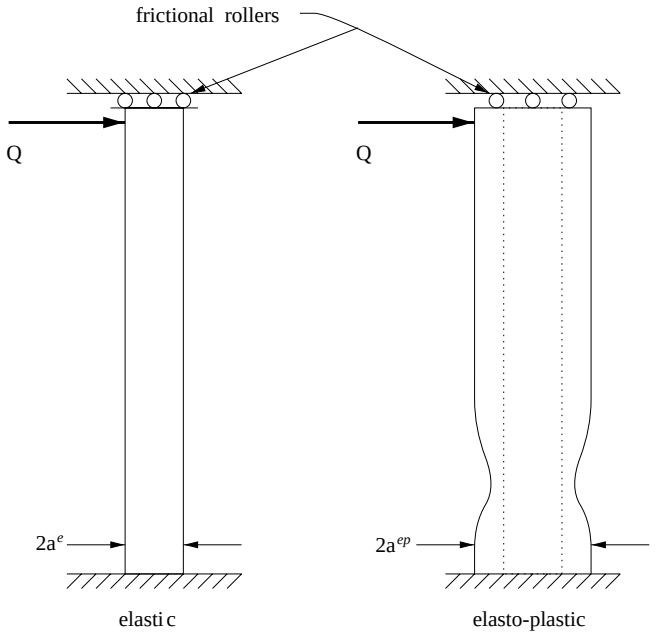

Fig. 15. Analogy to the effect of plastic deformation on the contact tangential stiffness using a column with changeable width.

Table 1
Numerical examples: force parameters for loading histories shown in Fig. 17

Loading history	$P_{\max}$ (N)	$Q_{\max}$ (N)	P_{Qbg} (N)	$\mu P_{\max}$ (N)
$\mathbb{A}$	1500	270	300	300
$\mathbb{B}$	500	90	100	100
$\mathbb{C}$	250	45	50	50

integration procedures, treatment of contact constraints, etc.) and into the mechanics of deformation under combined normal and tangential loading increase are required to shed some light into the nature of these bumps. In other words, were these bumps due to the implementation of numerical methods employed in ABAQUS, or were they actual behavior of the sphere under combined increase of normal and tangential loads well beyond the incipient yield limit?

3.2. Additive decomposition of elasto-plastic contact-area radius

In our previous papers, [1,2], the additive decomposition of elasto-plastic contact radius was introduced as an important step to construct an accurate elasto-plastic NFD model. Such a decomposition is also used in the construction of this proposed elasto-plastic TFD model to represent the effect of plastic deformation on the contact-area radius. That is, the elasto-plastic contact-area radius a^{ep} can be decomposed to be the sum of an elastic part a^{e} and a plastic part a^{p} as follows:

$$a^{\mathrm{ep}} = a^{\mathrm{e}} + a^{\mathrm{p}}, \tag{3.1}$$

where the elastic contact-area radius a^{e} is determined using Hertz theory by $(2.1)_1$ with the corresponding normal contact force. As observed from FEA results, the plastic part of the contact-area radius a^{p} can be approximated using a bilinear function as

$$a^{\mathrm{p}} = \begin{cases} C_a\langle P - P_{\mathrm{Y}}\rangle(m) & \text{for loading,} \\ C_a\langle P_{\max} - P_{\mathrm{Y}}\rangle(m) & \text{for unloading,} \end{cases} \tag{3.2}$$

where C_a is a constant that can be determined by the properties of the spheres in contact. For example, for the contact problem considered, our elasto-plastic FEA results give a C_a value of 2.33×10^{-7} m/N. We refer the readers to [1,22] for more details on the approximation (3.2) and FEA results. In (3.2), the symbol $\langle\rangle$ denotes the MacCauley bracket defined by

$$\langle x\rangle = \begin{cases} 0 & \text{for } x \leqslant 0, \\ x & \text{for } x > 0. \end{cases} \tag{3.3}$$

Replacing the contact-area radius a in (2.10) by the elasto-plastic contact-area radius a^{ep} defined in (3.1), we obtain

$$K_{\mathrm{T},0}^{\mathrm{ep}} = \frac{8Ga^{\mathrm{ep}}}{2-\nu}. \tag{3.4}$$

Since $a^{\mathrm{ep}} \geqslant a^{\mathrm{e}}$, the initial elasto-plastic tangential stiffness $K_{\mathrm{T},0}$ given by (3.4) is larger than that for elastic case given by (2.10). Fig. 13 shows the FEA results from a large plastic deformation resulting in an increased tangential stiffness. The importance of the additive decomposition (3.1) of the contact-area radius a^{ep} lies in the consistency between our successful elasto-plastic NFD model (proposed in [1,2]) and the present elasto-plastic TFD model. Such consistency is often lacking in the literature of granular flow simulations, where elasto-plastic deformation is accounted for only in the normal direction (in various

ways), while only elastic (frictional) deformation is accounted for in the tangential direction. (See, for example, [6,27,31].) In addition, the formalism of the additive decomposition of the contact-area radius is consistent with that employed in the continuum theory of elasto-plasticity. On the other hand, the additive decomposition (3.1) above is not sufficient to describe the decrease in the tangential stiffness when both the normal force P and the tangential force Q vary.

3.3. Equivalent elasto-plastic modulus E^{ep}

We introduce the equivalent elasto-plastic modulus E^{ep} to account for the weakening of tangential stiffness by plastic deformation. As described in [1], the irreversible plastic deformation flattens the contact surface, and thus increases the local radius of curvature of the sphere at the contact point; such change in the radius of curvature can be modeled as

$$R_{\mathrm{p}} = C_{\mathrm{R}}(P)R, \tag{3.5}$$

where $C_{\mathrm{R}}(P)$ is the coefficient for adjusting the radius of curvature to account for the plastic deformation. Noticing that the plastic deformation tends to flatten the contact surface, and that the larger the normal force P the larger the local radius of curvature at the contact point, we propose to approximate $C_{\mathrm{R}}(P)$ as

$$C_{\mathrm{R}}(P) = \begin{cases} 1.0 & \text{for } P \leqslant P_{\mathrm{Y}}, \\ 1.0 + K_{\mathrm{c}}\langle P - P_{\mathrm{Y}}\rangle & \text{for } P > P_{\mathrm{Y}}, \end{cases} \tag{3.6}$$

where K_{c} is a constant determined by the properties of the sphere in contact. For the sphere employed in our FEA, we obtain $K_{\mathrm{c}} = 2.69 \times 10^{-4}\ \mathrm{N}^{-1}$.

As documented in [1], we also observe that the relationship between the normal displacement and the radius of contact area follows the *parabola law*:

$$\alpha = \frac{(a^{\mathrm{ep}})^2}{R_{\mathrm{p}}}. \tag{3.7}$$

Recall that in [1] we assume the normal traction having the shape of a half ellipsoid on the contact surface. The elasto-plastic contact-area radius a^{ep} can thus be expressed using the Hertz theory (Eq. $(2.1)_1$) applied to an equivalent (or fictitious) sphere with radius of curvature R_{p} and with equivalent elastic modulus E^{ep} as follows:

$$a^{\mathrm{ep}} = \left(\frac{3PC_{\mathrm{R}}R_{\mathrm{p}}(1-\nu^2)}{4E^{\mathrm{ep}}}\right)^{1/3}. \tag{3.8}$$

From (3.8), the equivalent elastic modulus E^{ep} for the case in which the normal force P increases can be written as

$$E^{\mathrm{ep}} = \frac{3PC_{\mathrm{R}}R(1-\nu^2)}{4(a^{\mathrm{ep}})^3}. \tag{3.9}$$

For contact with plastic deformation, the equivalent elastic modulus E^{ep} is less than the Young's modulus, thus the equivalent shear modulus G^{ep} is decreased according to

$$G^{\mathrm{ep}} = \frac{E^{\mathrm{ep}}}{2(1+\nu)}. \tag{3.10}$$

For the case of normal force increasing, the equivalent shear modulus G^{ep} obtained with (3.9) and (3.10) is applied to (3.4) to calculate the initial elasto-plastic tangential stiffness

$$K_{\mathrm{T},0}^{\mathrm{ep}} = \frac{8G^{\mathrm{ep}}a^{\mathrm{ep}}}{2-\nu}. \tag{3.11}$$

The case in which normal force decreases is similar. When the normal force is decreasing, the initial tangential stiffness $K_{\mathrm{T},0}$ is also evaluated by (3.11). Considering that the unloading of the normal force is elastic with fixed plastic deformation, the expression for the equivalent elastic modulus takes the following form

$$E^{\mathrm{ep}} = \frac{3P(C_{\mathrm{R}})_{P=P_{\max}}R(1-\nu^2)}{4(a^{\mathrm{e}})^3}, \tag{3.12}$$

where $(C_{\mathrm{R}})_{P=P_{\max}}$ designates the value of the coefficient C_{R} at the maximum value of the normal force, and a^{e} the elastic contact radius determined by $(2.1)_1$, as per Hertz theory.

When the normal force is constant, the amount of plastic deformation is primarily determined by the normal force, based on our observations of the FEA results. It follows that the case of constant normal force is similar to the case of decreasing normal force.

4. Algorithm of the elasto-plastic TFD model

In this section, we present the computational algorithm and the pseudocode for the proposed elasto-plastic TFD model.

4.1. Elasto-plastic TFD model

As shown in Fig. 16, the normal pressure on the contact surface is almost constant inside the contact area. The FE maximum normal pressure $(p_{\mathrm{FE}})_{\max}$ on the contact surface is always slightly more than twice the yield stress of the material σ_{Y}, i.e., $p_{\max} \approx 2.3\sigma_{\mathrm{Y}}$, *regardless* of the level of normal contact force when $P \gg P_{\mathrm{Y}}$.

In the present elasto-plastic TFD model, we approximate the distribution of the normal pressure on the elasto-plastic contact surface by an elliptic curve represented by the dashed line in Fig. 16, and expressed by

$$p_{\mathrm{ep}}(r) = (p_{\mathrm{m}})_{\mathrm{ep}}\left[1-\left(\frac{r}{a^{\mathrm{ep}}}\right)\right]^{1/2}, \tag{4.1}$$

where $(p_{\mathrm{m}})_{\mathrm{ep}}$ is the maximum normal pressure for the proposed elasto-plastic TFD model; note that this approximation does not affect the elasto-plastic NFD relationship [1]. Recall that the integration of normal pressure on the contact surface is equal to the normal force P, i.e.,

$$P = \frac{2}{3}(p_{\mathrm{m}})_{\mathrm{ep}}\pi(a^{\mathrm{ep}})^2 \;\Rightarrow\; (p_{\mathrm{m}})_{\mathrm{ep}} = \frac{3P}{2\pi(a^{\mathrm{ep}})^2}. \tag{4.2}$$

For the case shown in Fig. 16, when $P = 1500$ N, we have $(p_{\mathrm{m}})_{\mathrm{ep}} \approx 3.2\times 10^8$ N/m^2. Comparing to the maximum normal pressure obtained using Hertz theory with the same level of normal force P, the value of $(p_{\mathrm{m}})_{\mathrm{ep}}$ is much smaller. This observation can be explained by the smaller equivalent elastic modulus E^{ep}.

As we already pointed out, the assumption of elliptic normal pressure distribution given by (4.1) does not affect the elasto-plastic NFD relationship, and plays an important role in the present elasto-plastic TFD

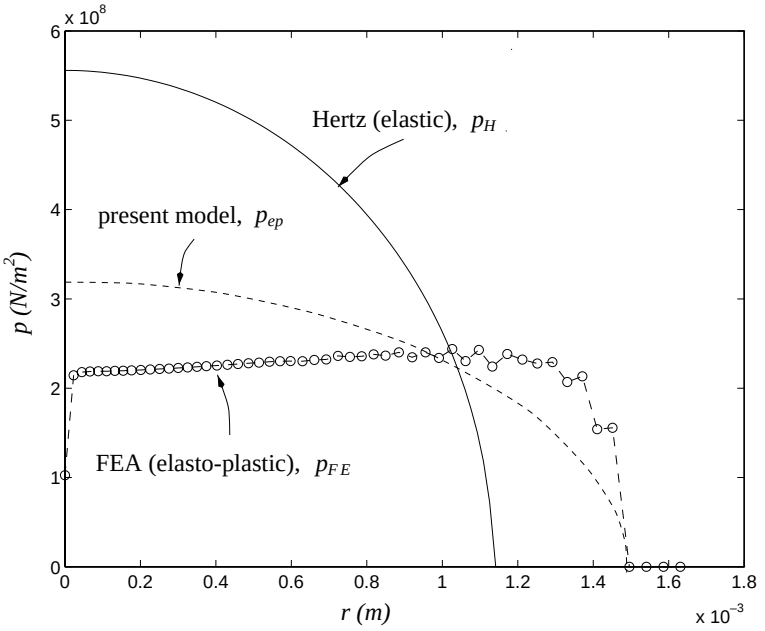

Fig. 16. Elasto-plastic frictional contact: normal stress distribution.

model. With the equivalent elliptic distribution of the normal pressure as expressed in (4.1), together with the reduced equivalent elastic modulus E^{ep}, the elasto-plastic TFD relation can now be constructed in a manner analogous to the elastic-frictional TFD relation proposed in [6].

When the normal force P is a constant, the relationship between Q_n for the previous time-step and Q_{n+1} for the current time-step is given by the following incremental formula

$$Q_{n+1} = Q_n + K^{\mathrm{ep}}_{\mathrm{T},n}\Delta\delta, \tag{4.3}$$

where $\Delta\delta$ is the increment of tangential displacement, $K^{\mathrm{ep}}_{\mathrm{T},n}$ the tangential stiffness coefficient for the elasto-plastic contact at the current increment step, which is computed as follows:

$$K^{\mathrm{ep}}_{\mathrm{T}} = \begin{cases} K^{\mathrm{ep}}_{\mathrm{T},0}\left(1 - \dfrac{Q_n - Q^*}{2\mu P}\right)^{1/3} & \text{for } Q \text{ increasing } (\nearrow) \text{ and } |Q_n| \leqslant |Q^*|, \\ K^{\mathrm{ep}}_{\mathrm{T},0}\left(1 - \dfrac{Q_n}{\mu P}\right)^{1/3} & \text{for } Q \text{ increasing } (\nearrow) \text{ and } |Q_n| > |Q^*|, \\ K^{\mathrm{ep}}_{\mathrm{T},0}\left(1 - \dfrac{Q^* - Q_n}{2\mu P}\right)^{1/3} & \text{for } Q \text{ decreasing } (\searrow) \text{ and } |Q_n| \leqslant |Q^*|, \\ K^{\mathrm{ep}}_{\mathrm{T},0}\left(1 + \dfrac{Q_n}{\mu P}\right)^{1/3} & \text{for } Q \text{ decreasing } (\searrow) \text{ and } |Q_n| > |Q^*|, \end{cases} \tag{4.4}$$

where $K^{\mathrm{ep}}_{\mathrm{T},0}$ is the initial tangential stiffness determined by (3.4) using a^{ep} and E^{ep}. Clearly, when $P \leqslant P_{\mathrm{Y}}$, the tangential stiffness $K^{\mathrm{ep}}_{\mathrm{T},0}$ has the same value as obtained using the MD [20] theory.

For the case where both P and Q are increasing simultaneously, we have two subcases. Let $\Delta P = P_{n+1} - P_n$ and $\Delta Q = Q_{n+1} - Q_n$. *Subcase 1*: When $\Delta Q \geqslant \mu\Delta P$, the tangential displacement is updated by (similar to (2.17))

$$\delta_{n+1} = \delta_n + \frac{\mu\Delta P}{(K^{\mathrm{ep}}_{\mathrm{T},0})_{P=P_n}} + \frac{\Delta Q - \mu\Delta P}{K^{\mathrm{ep}}_{\mathrm{T},n+1}}, \tag{4.5}$$

where the tangential stiffness is determined by (similar to (2.18))

$$K_{\mathrm{T},n+1}^{\mathrm{ep}} = \frac{8G^{\mathrm{ep}}a^{\mathrm{ep}}}{2-\nu}\left(1-\frac{Q_n+\mu\Delta P}{\mu P_{n+1}}\right)^{1/3}. \tag{4.6}$$

Subcase 2: When $\Delta Q < \mu\Delta P$, the tangential displacement is updated by (similar to (2.21))

$$\delta_{n+1} = \delta_n + \frac{\Delta Q}{(K_{\mathrm{T},0}^{\mathrm{ep}})_{P=P_n}}. \tag{4.7}$$

For the other loading cases (P decreasing, Q increasing; P increasing, Q decreasing; P decreasing, Q decreasing), we refer the readers to [6] for more details.

4.2. Pseudocode: force-driven version

We summarize the force-driven version of the proposed elasto-plastic TFD model in Algorithm 4.1 below.

Algorithm 4.1. *Elasto-plastic TFD model*: force-driven version.

Input: $R, E, \nu, \sigma_{\mathrm{Y}}$.
Calculated P_{Y} via the elasto-plastic NFD model.
Data: Normal forces: P_n, P_{n+1}, and $P_{\max}$ etc.
Calculated $a_{n+1}^{\mathrm{e}}, a_{n+1}^{\mathrm{p}}$, and a_{n+1}^{ep}.
Initialization: Set $Q_0^* = 0$, $Q_{\mathrm{inc}} =$ **true**.
Data: Force Q_n, and Q_{n+1}, displacement δ_n, and Q_n^*.
Goal: Compute next tangential displacement δ_{n+1}.
Calculate $\Delta P_{n+1} = P_{n+1} - P_n$ and $\Delta Q_{n+1} = Q_{n+1} - Q_n$.
Set $Q_{n+1}^* = Q_n^*$.
① **if** $\Delta P_{n+1} = 0$ (P constant)
② **if** $P_{n+1} \leqslant P_{\mathrm{Y}}$ (elastic)
Calculate $K_{\mathrm{T},0}$ via (2.10).
② **elseif** $P_{n+1} > P_{\mathrm{Y}}$ (plastic)
Calculate $(E^*)^{\mathrm{ep}}$ via (3.12).
Calculate $K_{\mathrm{T},0}^{\mathrm{ep}}$ via (3.11).
② **endif**
③ **if** $\Delta Q_{n+1} \geqslant 0$ (Q increasing)
Calculate $K_{\mathrm{T},n}^{\mathrm{ep}}$ via (4.4);
Calculate δ_{n+1} via (4.3).
Set $Q_{\mathrm{inc}} =$ **true**.
③ **elseif** $\Delta Q_{n+1} < 0$ (Q decreasing)
if $Q_{\mathrm{inc}} =$ **true**
Set $Q_{n+1}^* = Q_n$.
endif
Calculate $K_{\mathrm{T},n}^{\mathrm{ep}}$ via (4.4);
Calculate δ_{n+1} via (4.3).
Set $Q_{\mathrm{inc}} =$ **false**.
③ **endif**
① **elseif** $\Delta P_{n+1} > 0$ (P loading)

④ **if** $P_{n+1} \leqslant P_Y$ (elastic)
Calculate $K_{T,0}$ via (2.10).
④ **elseif** $P_{n+1} > P_Y$ (plastic)
Calculate $(E^*)^{ep}$ via (3.9);
Calculate $K^{ep}_{T,0}$ via (3.11).
④ **endif**
⑤ **if** $\Delta Q_{n+1} \geqslant 0$ (Q increasing)
⑥ **if** $\Delta Q_{n+1} \geqslant \mu \Delta P$
Calculate $K^{ep}_{T,n+1}$ via (4.6);
Calculate δ_{n+1} via (4.5).
⑥ **elseif** $\Delta Q_{n+1} < \mu \Delta P$
Calculate δ_{n+1} via (4.7).
WARNING: NOT a simple loading step.
⑥ **endif**
Set $Q_{inc} =$ **true**.
⑤ **elseif** $\Delta Q_{n+1} < 0$ (Q decreasing)
Set $Q_{inc} =$ **false**.
⑤ **endif**
① **elseif** $\Delta P_{n+1} < 0$ (P unloading)
⑦ **if** $P_{n+1} \leqslant P_Y$ (elastic)
Calculate $K_{T,0}$ via (2.10).
⑦ **elseif** $P_{n+1} > P_Y$ (plastic)
Calculate $(E^*)^{ep}$ via (3.12).
Calculate $K^{ep}_{T,0}$ via (3.11).
⑦ **endif**
⑧ **if** $\Delta \delta_{n+1} \geqslant 0$ (Q increasing)
Set $Q_{inc} =$ **true**.
⑧ **elseif** $\Delta \delta_{n+1} < 0$ (Q decreasing)
Set $Q_{inc} =$ **false**.
⑧ **endif**
① **endif**

5. Numerical examples

We implemented the present elasto-plastic TFD model in a MATLAB code. The TFD curves produced by using the present TFD model are compared against the corresponding curves from 3-D FEA results for the static contact of two identical aluminum spheres. Elasto-plastic frictional FEA were performed for the loading histories shown in Fig. 17 and Table 1. The mechanical properties and the FE model were the same as described in Sections 2.2 and 3.1. The TFD curves (Q versus δ) from (i) The MD [20] theory, (ii) FEA, and (iii) the present elasto-plastic TFD model shown in Figs. 18, 20, and 21. All figures are produced from force-driven procedures, i.e., the tangential and normal forces are provided as input, and the tangential and normal displacements are obtained as output. The coefficients of restitution in the tangential direction shown in Figs. 18, 20, and 21 (denoted by β_{FE} for FEA results, by β_{PM} for the present TFD model, and by β_{MD} for the MD [20] theory), are obtained as the square of energy dissipation in the corresponding loading path, computed by

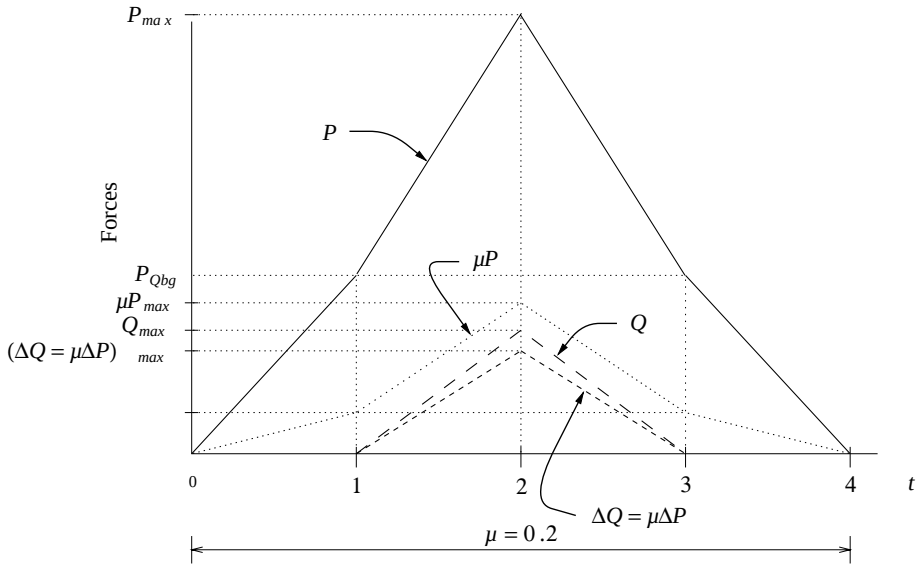

Fig. 17. Numerical examples: loading histories for comparison of TFD curves.

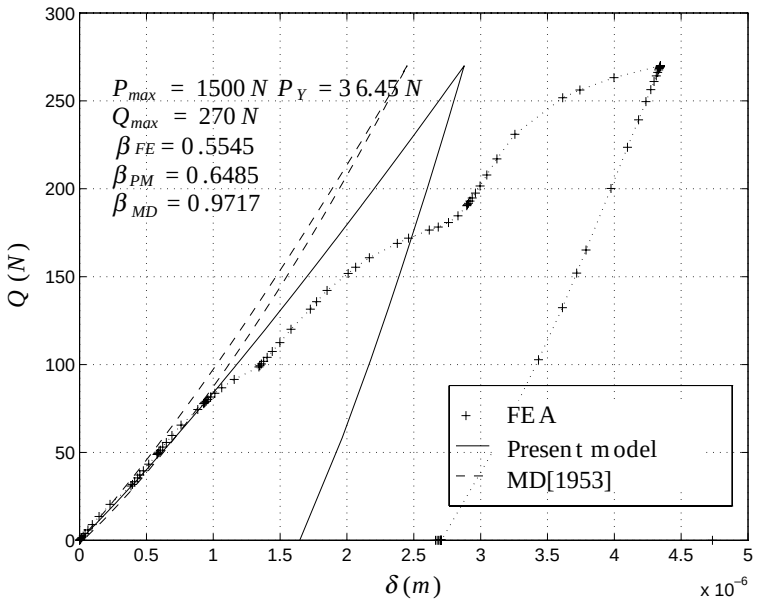

Fig. 18. Elasto-plastic frictional contact: loading history 𝔸. TFD curves. Comparison of present force-driven TFD model to [20] and to force-driven FEA.

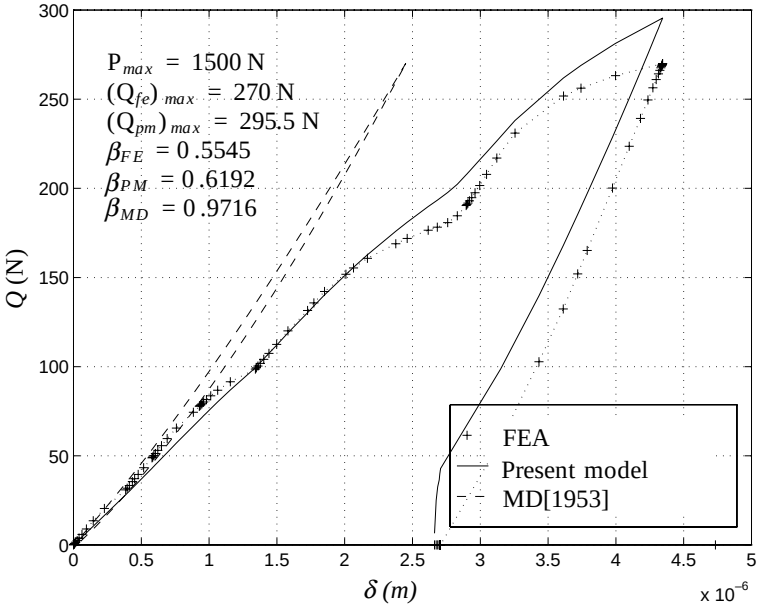

Fig. 19. Elasto-plastic frictional contact: Loading history $\mathbb{A}$. TFD curves. Comparison of the displacement-driven version of the proposed TFD model to other models.

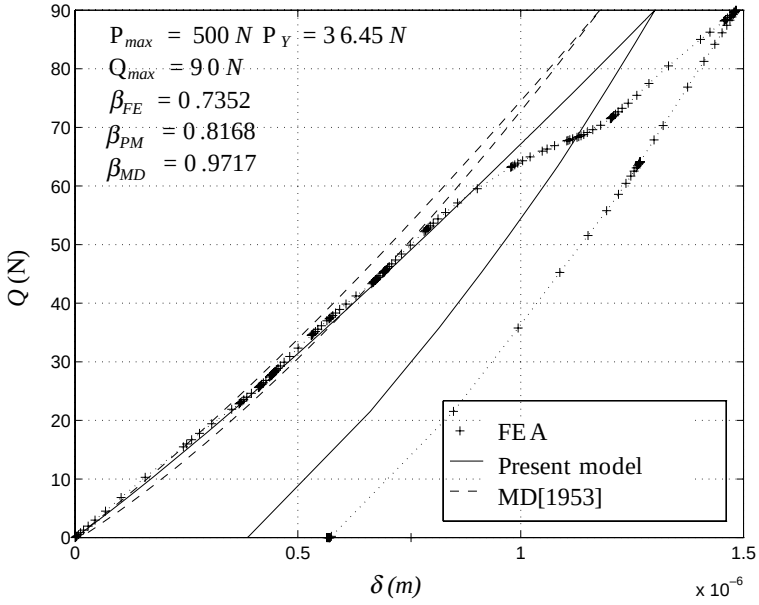

Fig. 20. Elasto-plastic frictional contact: Loading history $\mathbb{B}$. TFD curves. Comparison of the present force-driven TFD model to the MD [20] model and to FEA.

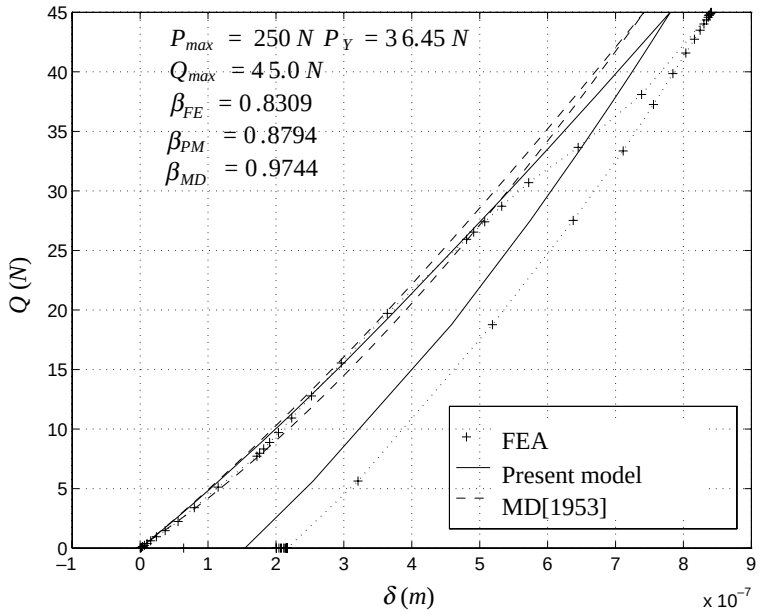

Fig. 21. Elasto-plastic frictional contact: loading history $\mathbb{C}$. TFD curves. Comparison of the present force-driven TFD model to the MD [20] model and to FEA.

$$\beta := \left(\frac{\text{Area under tangential unloading curve}}{\text{Area under tangential loading curve}} \right)^{1/2} = \left(\frac{\displaystyle\sum_{i\,\text{s.t.}\,\{\delta_i-\delta_{i-1}>0\}}^{\text{loading}} \frac{1}{2}(\delta_i-\delta_{i-1})(Q_i+Q_{i+1})}{\displaystyle\sum_{j\,\text{s.t.}\,\{\delta_j-\delta_{j-1}<0\}}^{\text{unloading}} -\frac{1}{2}(\delta_j-\delta_{j-1})(Q_j+Q_{j+1})} \right)^{1/2} . \tag{5.1}$$

Fig. 18 shows the Q versus δ curves under varying normal force P with $P_{\max} = 1500$ N (loading history $\mathbb{A}$ in Fig. 17 and Table 1). It can be seen that the curve produced by the present elasto-plastic TFD model can more accurately account for the effect of plastic deformation, compared to the TFD curve produced by the MD [20] theory. Even though there are large errors in the tangential displacement for the same level of tangential force, the slopes of the loading and unloading parts of the TFD curve produced by the present TFD model agree closely with the main slopes of the TFD curve from the FEA results.

As mentioned earlier, the bumps are likely the results of some sliding mechanism. If this sliding mechanism were eliminated in the loading curve in the FEA results, one can easily see that the FEA results will be brought closer to results of the proposed elasto-plastic TFD model. Essentially, the horizontal distance that separates the two unloading curves (FEA results and present TFD model) is roughly the cumulative amount of sliding that occurs during the loading stage. The causes for the sliding mechanism (and thus the "bumps" mentioned earlier in relation to Fig. 14 in Section 3) require further investigation.

The tangential coefficient of restitution from the present TFD model is $\beta_{\text{PM}} = 0.6485$, which differs from the FEA result ($\beta_{\text{FE}} = 0.5545$) by 16.9%. Even though further work still needs to be done to more accurately account for the effects of plastic deformation on the TFD relation, the present work is a first attempt

at producing a good elasto-plastic TFD model that is consistent with our successful elasto-plastic NFD model, considering that there has been no previous work on this topic in literature.

Another way to verify the workability of the present elasto-plastic TFD model even in the presence of additional sliding mechanism is to turn to the displacement-driven version of the present TFD model, and to use as input the tangential displacement obtained from elasto-plastic force-driven FEA. In this manner, the additional sliding mechanism is included naturally in the tangential-displacement time history that serves as input data.

The results shown in Fig. 19 agree well with FEA results. The reason was because the input tangential displacement (obtained from FEA) contained the additional sliding mechanism (bumps), and the proposed elasto-plastic TFD model reproduces well the tangential force. We note that in simulations using the DEM, the displacement-driven versions of both NFD model and TFD model are used [2,32]. It follows that the proposed elasto-plastic TFD model is quite accurate for DEM simulations.

Figs. 20 and 21 are two more comparisons between the present elasto-plastic TFD model and FEA results. The TFD curves produced by the present TFD model are closer to the FEA results in terms of tangential displacement δ, since there are fewer 'bumps' and the 'bumps' are smaller on the FEA TFD curves than that of the case shown in Fig. 18. The slopes of the TFD curves produced by the present TFD model, again, agree closely with that of the TFD curves from the FEA results. Again, if the additional sliding mechanism that gave rise to the bumps were eliminated, we have good agreement between the FEA results and the present TFD model, as the distance separating the unloading curves is essentially the amount of sliding that occurred.

The results reported in Figs. 20 and 21 also show good agreement in the energy dissipation ratios, as computed using both FEA and the present TFD model. For the loading path $\mathbb{B}$ (see Fig. 17 and Table 1), the tangential coefficient of restitution by the present TFD model ($\beta_{\mathrm{PM}} = 0.8168$) differs from that obtained with FEA results ($\beta_{\mathrm{FE}} = 0.7352$) by 11.1% (see Fig. 20). For the loading path $\mathbb{C}$, the results are $\beta_{\mathrm{PM}} = 0.8794$ and $\beta_{\mathrm{FE}} = 0.8309$, and thus the difference is only 5.8% (see Fig. 21).

6. Closure

We have presented an elasto-plastic frictional TFD model that accounts for the effect of plastic deformation. The construction of an elasto-plastic frictional TFD model is a more challenging undertaking than the construction of an elasto-plastic NFD model. Our proposed elasto-plastic frictional TFD model is based on the analysis of FEA results, and on a generalization of elastic-frictional contact mechanics theories (Hertz theory and CMD theory) to the plastic regimes. The methodology of this proposed TFD model is consistent with the successful elasto-plastic NFD model proposed in [1,2]. A comparison between the results obtained using the present TFD model and the FEA results shows that the present TFD model can quantitatively account for the effect of plastic deformation on the TFD relationship.

We note that the accuracy of a TFD model plays an important role in granular-flow simulations, as it has been amply demonstrated in [6] that different TFD models yield starkly different results, such as the important statistics on collision frequency and contact force amplitude. It is therefore important to use an accurate TFD model.

Although there are some plastic deformation effects that are still to be accounted for, the results shown have proved that the present elasto-plastic TFD model is superior to other existing models, and is the first model to account for plastic deformation in the TFD relationship. [5] Future work will focus on investigating the behavior of the "bumps" observed in FEA, and to improve the present TFD model if necessary. We

[5] Again, we refer the readers to footnote 4 and to Refs. [35,36].

note that the displacement-driven version of the present model produces accurate results. Such accuracy is important for simulation by the DEM, which employs the displacement-driven versions of the FD models. We refer the readers to [32] for the details of the displacement-driven version of this TFD model.

Finally, we also note that the present formalism will be helpful in the generalization of the proposed elasto-plastic frictional NFD and TFD models to account for *viscous effects*, i.e., elasto-*visco*-plasticity, in colliding particles (e.g., biological materials [33,34]). Another important generalization is the case of particles of different sizes and shapes.

Acknowledgements

The support of the National Science Foundation is gratefully acknowledged.

References

[1] L. Vu-Quoc, X. Zhang, L. Lesburg, A normal force–displacement model for contacting spheres accounting for plastic deformation: force-driven formulation, ASME Journal of Applied Mechanics 67 (2) (2000) 363–371.
[2] L. Vu-Quoc, X. Zhang, An elasto-plastic contact force–displacement model in the normal direction: displacement-driven version, Proceedings of the Royal Society of London, Series A 455 (1991) (1999) 4013–4044.
[3] M. Bursik, B. Martinez-Hackert, H. Delgado, A. Gonzalez-Huesca, A smoothed-particle hydrodynamic automaton of landform degradation by overland flow, Geomorphology 53 (1–2) (2003) 25–44.
[4] T. Mullin, Mixing and de-mixing, Science 295 (5561) (2002) 1851–1851.
[5] M. Buchanan, Think outside the sandbox, Nature 425 (2003) 556–557.
[6] L. Vu-Quoc, X. Zhang, An accurate and efficient tangential force–displacement model for elastic-frictional contact in particle-flow simulations, Mechanics of Materials 31 (1999) 235–269.
[7] P. Cleary, Modelling communition devices using DEM, International Journal for Numerical and Analytical Methods in Geomechanics 25 (1) (2001) 83–105.
[8] L.G. Austin, A treatment of impact breakage of particles, Powder Technology 126 (1) (2002) 85–90.
[9] L. Vu-Quoc, X. Zhang, O.R. Walton, A 3-D discrete element method for dry granular flows of ellipsoidal particles, Computer Methods in Applied Mechanics and Engineering 187 (3–4) (2000) 483–528 (Invited paper for the special issue on *Dynamics of Contact/Impact Problems*, edited by D. Benson).
[10] N.V. Brilliantov, F. Spahn, J.M. Hertzsch, T. Poschel, Model for collisions in granular gases, Physical Review E 53 (5) (1996) 5382–5392.
[11] H.M. Jaeger, S.R. Nagel, Physics of the granular state, Science 255 (5051) (1992) 1523–1531.
[12] F.G. Bridges, A. Hatzes, D.N.C. Lin, Structure, stability and evolution of Saturn's rings, Nature 309 (5966) (1984) 333–335.
[13] M. Rhein, R. Barth, E. Ditzel, H. Feldmeier, E. Kankeleit, V. Lips, C. Muntz, W. Norenberg, H. Oeschler, A. Piechaczek, W. Polai, I. Schall, Elastoplasticity in dissipative heavy-ion collisions, Physical Review C 49 (1) (1994) 250–265.
[14] L. Bureau, T. Baumberger, C. Caroli, Shear response of a frictional interface to a normal load modulation, Physical Review E 62 (5) (2000) 6810–6820.
[15] F.M. Borodich, Comment on "elastoplastic contact between randomly rough surfaces", Physical Review Letters 88 (6) (2002) (Article no. 069601).
[16] S.B. Savage, Analyses of slow high-concentration flows of granular materials, Journal of Fluid Mechanics 377 (1998) 1–26.
[17] L. Bocquet, W. Losert, D. Schalk, T.C. Lubensky, J.P. Gollub, Granular shear flow dynamics and forces: experiment and continuum theory, Physical Review E 6501 (1) (2002) (Article no. 011307).
[18] X. Zhang, L. Vu-Quoc, Modeling the dependence of the coefficient of restitution on the impact velocity in elasto-plastic collisions, International Journal of Impact Engineering 27 (3) (2002) 317–341.
[19] K.L. Johnson, Contact Mechanics, second ed., Cambridge University Press, New York, 1985.
[20] R.D. Mindlin, H. Deresiewicz, Elastic spheres in contact under varying oblique forces, ASME Journal of Applied Mechanics 20 (September) (1953) 327–344.
[21] C.W. Shih, W.S. Schlein, J.C.M. Li, Photoelastic and finite element analysis of different size spheres in contact, Journal of Materials Research 7 (4) (1992) 1011–1017.
[22] L. Vu-Quoc, X. Zhang, L. Lesburg, Normal and tangential force–displacement relations for frictional elasto-plastic contact of spheres, International Journal of Solids and Structures 38 (36–37) (2001) 6455–6490.

[23] G.B. Sinclair, P.S. Follansbee, K.L. Johnson, Quasi-static normal indentation of an elasto-plastic half-space by a rigid sphere. ii. Results, International Journal of Solids and Structures 21 (8) (1985) 865–888.
[24] E.R. Kral, K. Komvopoulos, D.B. Bogy, Elastic-plastic finite element analysis of repeated indentation of a half-space by a rigid sphere, ASME Journal of Applied Mechanics 60 (1993) 829–841.
[25] R. Dobry, E. Petrakis, A. Seridi, General model for contact law between two rough spheres, ASCE Journal of Engineering Mechanics 117 (6) (1991) 1365–1381.
[26] O.R. Walton, R.L. Braun, Viscosity, granular-temperature, and stress calculations for shearing assemblies of inelastic, frictional disks, Journal of Rheology 30 (5) (1986) 949–980.
[27] C. Thornton, C.W. Randall, Applications of theoretical contact mechanics to solid particle system simulation, in: M. Satake, J.T. Jenkins (Eds.), Micromechanics of Granular Materials, Elsevier Science Publishers B.V., Amsterdam, Netherlands, 1988, pp. 133–142.
[28] C. Cattaneo, Sul contatto di due corpi elastici: distribuzione locale degli sforzi, Accademia dei Lincei, Rendicotti 27 (6) (1938) 342–348.
[29] R.D. Mindlin, Compliance of elastic bodies in contact, ASME Journal of Applied Mechanics 16 (1949) 259–268.
[30] J. Jaeger, Elastic Impact with Friction, PhD thesis, Delft University, Netherlands, October 1992.
[31] O.R. Walton, Numerical simulation of inelastic, frictional particle–particle interactions, in: M.C. Roco (Ed.), Particulate Two-Phase Flow, Butterworth-Heinemann, Stoneham, MA, 1993, pp. 884–911, chapter 25.
[32] L. Vu-Quoc, X. Zhang, A new tangential force–displacement model for elasto-plastic frictional contact: displacement-driven version, Proceedings of the Royal Society of London Series A, submitted for publication.
[33] S. Gan-Mor, N. Galili, Rheological model of fruit collision with an elastic plate, Journal of Agricultural Engineering Research 75 (2) (2000) 139–147.
[34] R. Mathew, G.M. Hyde, Potato impact damage thresholds, Transactions of the ASAE 40 (3) (1997) 705–709.
[35] L. Lesburg, Toward a Realistic and Consistent Force-Displacement Model for Discrete Element Simulation of Dry Particle Systems, Master's thesis, University of Florida, Aug 1997.
[36] X. Zhang, On Computer Simulation of Dry Particle Systems using Discrete Element Method and the Development of DEM Contact Force-Displacement Models, PhD thesis, University of Florida, Dec 1998.